A NEW TURBULENT THREE-DIMENSIONAL FSI BENCHMARK FSI-PFS-3A: DEFINITION AND MEASUREMENTS

Andreas Kalmbach, Guillaume De Nayer and Michael Breuer

Professur für Strömungsmechanik (PfS), Helmut–Schmidt–Universität Hamburg
Holstenhofweg 85, D–22043 Hamburg, Germany
e-mail: kalmbach / denayer / breuer@hsu-hh.de

Keywords: FSI, experimental investigation, PIV, turbulent flow, three-dimensional benchmark case

Abstract. *In the last decade, the demand for the prediction of complex multi-physics problems such as fluid-structure interaction (FSI) has strongly increased. For the development and improvement of appropriate numerical tools several test cases were designed in order to validate the numerical results based on experimental reference data [4, 12, 13, 8, 9, 10]. Since FSI problems often occur in turbulent flows also in the experiments similar conditions have to be provided. In the test-case FSI-PfS-1a [7] presented in the first contribution to this session, a cylinder is used with an attached flexible rubber plate. The resulting FSI problem is nearly two-dimensional regarding the phase-averaged flow and the structure deformations. The actual test case FSI-PfS-3a is the reasonable further development step of this two-dimensional benchmark to a forced fully three-dimensional flow, which now also leads to a significant three-dimensional structure deformation. The cylinder is replaced by a truncated cone. Similar to FSI-PfS-1a [7] a rubber plate is attached at the backside. This geometrical setup is exposed to a constant flow at Re = 32,000 which is in the subcritical regime. Due to the linearly increasing diameter of the cone the alternating eddies in the wake even become larger resulting in correspondingly increasing structural displacements. Owing to these challenging flow and structure effects, this benchmark will be the next step for validating FSI predictions for real applications. The experiments are performed in a water channel with clearly defined and controllable boundary and operating conditions. For measuring the flow a two-dimensional mono-particle-image velocimetry (PIV) system is applied. In order to characterize the three-dimensional behavior of the flow, phase-averaged PIV measurements are performed at three different planes. The structural deformations are measured along a line on the structure surface with a time-resolved laser distance sensor. The resulting FSI problem shows a quasi-periodic deformation behavior so that a phase averaging of the results is reasonable. By phase-averaging turbulent fluctuations are averaged out and thus a comparison with corresponding numerical simulations based on LES [3] and RANS [12, 13] approaches is possible.*

1 INTRODUCTION

Numerical predictions play more and more an important role in most engineering fields due to the high costs of experiments and the rise of computational resources. Furthermore, engineering problems tackled by numerical simulations always have become more challenging and nowadays often involve so-called multi-physics applications. Fluid and structure interaction (FSI) is an example of such a multi-physics engineering field: A rigid but elastically mounted body or a deformable structure, such as a rotor blade or a membranous awning, is exposed to a fluid flow. The fluid forces acting on the structure move or deform it. These displacements or deflections modify the flow resulting in a coupling process between the fluid and the structure.

The Department of Fluid Mechanics of HSU Hamburg is working on the long-term objective of coupled simulations of big lightweight structures such as thin membranes exposed to turbulent flows (outdoor tents, awnings...). In order to approach this goal, a FSI code was developed and the validation process is presented for example in [3]. The FSI program is based on two separate highly specialized solvers (one for the fluid, one for the structure) coupled by a third code. Both solvers were at first checked and validated separately. Then, the full multi-physics program was tested considering a laminar FSI benchmark [17, 18]. A 3D turbulent test case, denoted FSI-LES, was also taken into account to prove the applicability of the newly developed coupling scheme in the context of large-eddy simulations (LES). However, the validation was not complete, because of the lack of experimental data to compare with.
For this purpose several FSI test cases were recently developed. In the test-case FSI-PfS-1a [7] presented in the first contribution to this session, a cylinder is used with an attached flexible rubber plate. The resulting FSI problem is nearly two-dimensional regarding the phase-averaged flow and the structure deformations in the first swiveling mode. Detailed comparisons between experimental measurements and numerical LES predictions were carried out [7]. Another test case, denoted as FSI-PfS-2a [13], showed more complex swiveling behavior in the second mode which is achieved by applying a steel weight to the configuration of FSI-PfS-1a. This test case was also investigated by experimental measurements and numerical URANS predictions. The actual test case, FSI-PfS-3a, is the reasonable further development step of these two-dimensional benchmarks to a forced fully three-dimensional flow, which now also leads to a significant three-dimensional structure deformation. Therefore, the goal of this paper is to present a turbulent FSI test case relying on detailed experimental investigations for the deformation of the structure and the flow field carried out at PfS Hamburg.

The paper is organized as follows: The new test case is completely described in Section 2. The experimental investigations including the water tunnel and the measuring techniques are presented in Section 3. Due to cycle-to-cycle variations of the FSI phenomenon observed in the experiment and in the simulation, the results have to be phase-averaged prior to a detailed comparison. The process is given in Section 4. Finally, the experimental results are presented and discussed in Section 5.

2 DESCRIPTION OF THE TEST CASE FSI-PfS-3a

The fluid-structure interaction test case described in this paper is denoted FSI-PfS-3a. It is composed of a flexible thin structure with a distinct thickness h clamped behind a fixed rigid non-rotating truncated cone installed in a water channel (see Fig. 1). The mildly tapered cone (ratio $D_2/D_1 = 1.5$) has a central position in the experimental test section, which yields a blocking ratio of about 12.2 %. The geometrical dimensions are resumed in Table 1. In the experimental setup the sketched section of the water channel is turned 90 degrees. Therefore,

the gravitational acceleration g points in x-direction in Fig. 1. In the experiment the flexible structure has a width w slightly smaller than the width of the test section W. Hence a small gap of about 1.5 mm exists between the side of the deformable structure and both lateral channel walls.
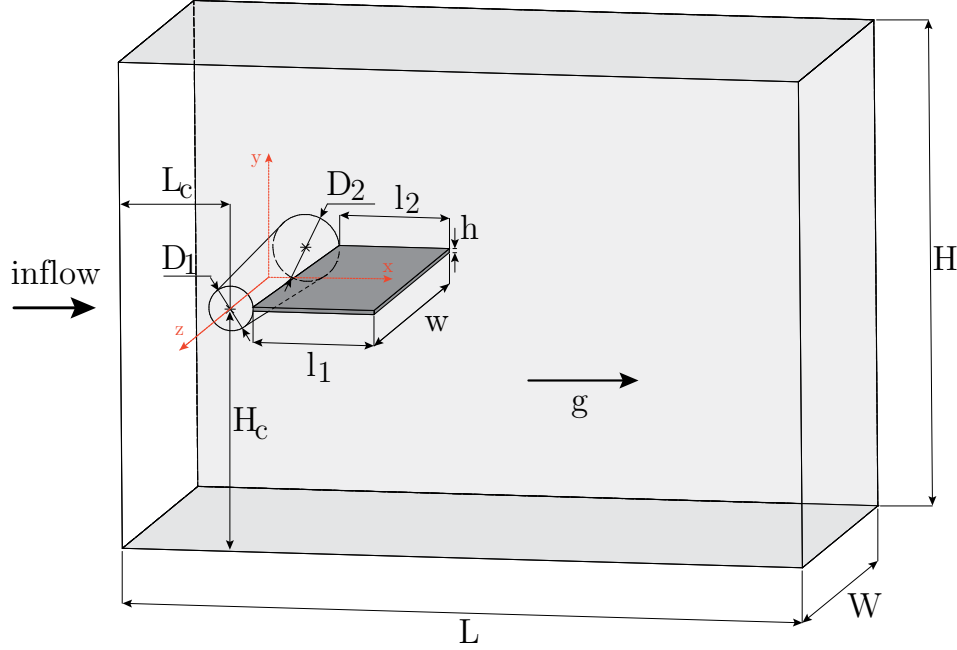

Figure 1: Sketch of the geometrical configuration of the benchmark case FSI-PfS-3a.

Small cone diameter	$D_1 = D$	$= 0.022$ m	
Large cone diameter	D_2	$= 0.033$ m	$D_2/D_1 = 1.5$
Cone center x-position	L_c	$= 0.077$ m	$L_c/D_1 = 3.5$
Cone center y-position	H_c	$= H/2 = 0.120$ m	$H_c/D_1 \approx 5.45$
Test section length	L	$= 0.338$ m	$L/D_1 \approx 15.36$
Test section height	H	$= 0.240$ m	$H/D_1 \approx 10.91$
Test section width	W	$= 0.180$ m	$W/D_1 \approx 8.18$
Long deformable structure length	l_1	$= 0.060$ m	$l/D_1 \approx 2.72$
Short deformable structure length	l_2	$= 0.0545$ m	$l/D_1 \approx 2.22$
Deformable structure thickness	h	$= 0.0021$ m	$h/D_1 \approx 0.09$
Deformable structure width	w	$= 0.177$ m	$w/D_1 \approx 8.05$

Table 1: Geometrical configuration of the FSI-PfS-3a benchmark.

The fluid used is water with an inflow velocity of $u_{\text{inflow}} = 0.969$ m/s. All experiments were performed under standard conditions at $T = 20°$C ($\rho_f = 998.20 \, \text{kg m}^{-3}$, $\mu = 1.0 \cdot 10^{-3}$ Pa s). Based on the inflow velocity chosen and the cone diameter D_1 and D_2 the Reynolds number of the experiment is equal to $Re_{D1} = 2.13 \cdot 10^4$ and $Re_{D2} = 3.20 \cdot 10^4$, respectively. The material used for the flexible structure is rubber with a density $\rho_s = 1360 \, \text{kg m}^{-3}$, a Young's modulus $E = 16$ MPa and a Poisson's ratio $\nu = 0.48$.

3 EXPERIMENTAL INVESTIGATIONS

The experimental investigations are carried out in the fluid mechanics lab of PfS with the help of a water channel, a particle-image velocimetry (PIV) system and a laser distance sensor. Several preliminary tests are performed to find the best working conditions in terms of good reproducibility of the results within the turbulent flow regime.

3.1 Description of the Water Channel and of the Flow

The water channel (Göttingen type, see Fig. 2) was designed and built at LSTM Erlangen [8, 9, 10] within the DFG research unit FOR 493 [5]. The channel ($2.8\,\mathrm{m}\ \times\ 1.3\,\mathrm{m}\ \times\ 0.5\,\mathrm{m}$, fluid volume of $0.9\,\mathrm{m}^3$) has a rectangular flow path and includes several rectifiers and straighteners to guarantee a uniform inflow into the test section. This test section has the geometry as described in Section 2 and possesses windows on three sides to allow optical measurement systems such as particle-image velocimetry. The structure (here the cone) is attached on the backplate of the test section and additionally fixed at the front glass plate. The water is put in motion by a $24\,\mathrm{kW}$ axial pump.
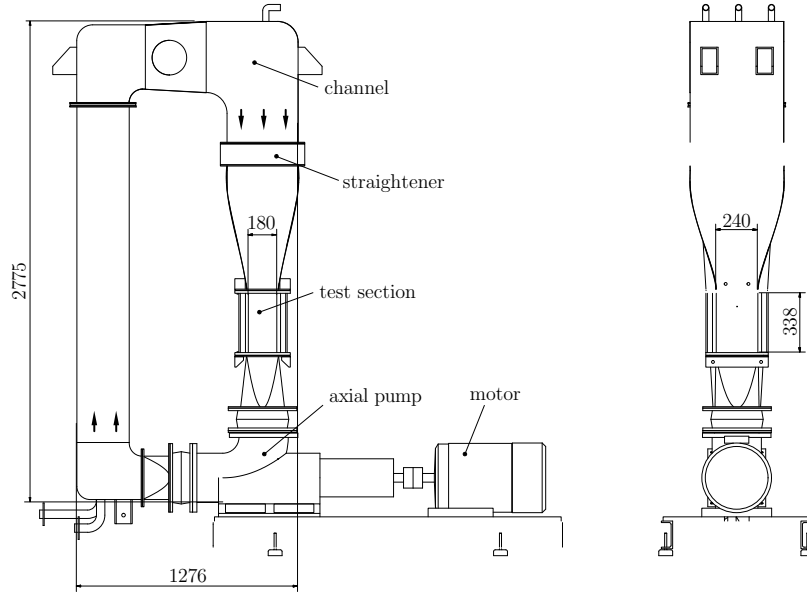

Figure 2: Sketch of the water channel (dimensions given in mm).

Based on the inflow velocity and the corresponding Reynolds number chosen, the flow around the cone is in the subcritical regime. Consequently, the boundary layers are still laminar, but transition to turbulence takes place in the free shear layers evolving from the separated boundary layers behind the apex of the cone. In the inflow section the velocity fields were measured by a laser-Doppler velocimetry system and was found to be nearly uniform except of course at the section walls. Furthermore, a low inflow turbulence level was measured ($\mathrm{Tu}_{\mathrm{inflow}} = 0.022$).

3.2 Measuring Techniques

The experimental investigations for a FSI problem have to describe both, the structure and the fluid coupled in time. In [8] the same camera was used to get the velocity fields and the

structural deflections. This method only works well for 2D FSI problems. In the present paper the turbulent flow regime causes cycle-to-cycle variations and significant three-dimensional deformations of the structure. Therefore, the displacement of the shell can not be extracted from the PIV images and a laser distance sensor is used instead. A 2D particle-image velocimetry (PIV) setup is applied to capture the velocity fields of the flow at three xy-planes at $(z/D)_{large} = -2.72$, $(z/D)_{middle} = 0$ and $(z/D)_{small} = 2.72$.

3.2.1 Particle-Image Velocimetry Setup

The particle-image velocimetry setup (cf. Adrian [1]) is classical: A single CCD camera measures the two components of the fluid velocity within the planar section illuminated by a laser light sheet (see Fig. 3). To assure a uniform illumination in front of and especially behind the structure, it was necessary to light up the flow field from both sides. The simultaneous illumination is realized by splitting the laser beam. Most of the flow field is illuminated by the first beam, which is directly coupled into a light sheet optic. The second beam is redirected by three specific laser mirrors to the other side of the test section forming a second light sheet on the backward region. The fluid is laden by small particles, which are following the flow and reflect the laser light. By taking two images of the reflection fields in a short time interval Δt, a cross-correlation technique can estimate the displacement of the particles using an equidistant grid. Using these displacements and the time interval Δt the velocity field in the illuminated plane can be calculated.
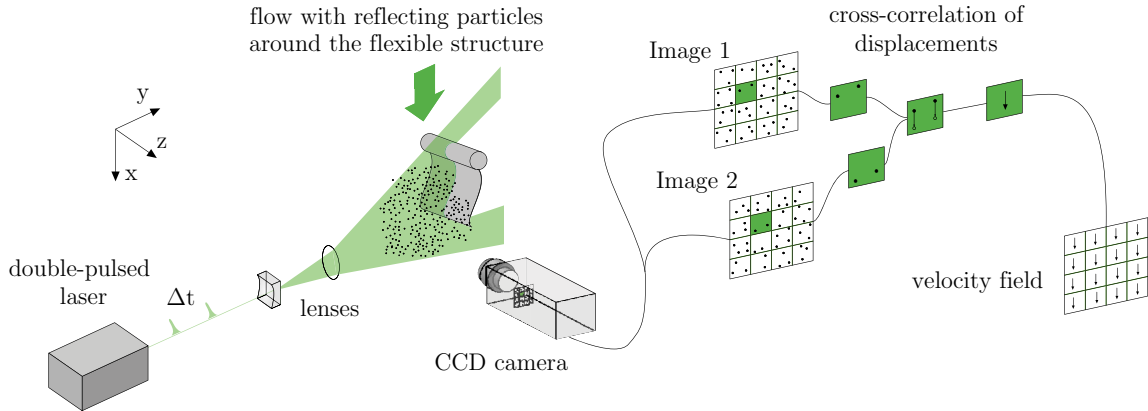

Figure 3: Measuring principle of a two-component PIV setup for the flow around the flexible structure.

Phase-resolved PIV-measurements (PR-PIV) are used to generate phase-averaged fluid velocity fields involving the structure deflections (see Section 4). The PR-PIV is carried out with a 4 Mega-pixel camera (TSI Powerview 4MP, charge-coupled device (CCD) chip) and a pulsed dual-head Neodym:YAG laser (Litron NanoPIV 200) with an energy of $200\,\mathrm{mJ}$ per laser pulse. The time between the frame-straddled laser was set to $\Delta t = 600\,\mu\mathrm{s}$. Laser and camera are controlled by a TSI synchronizer (TSI 610035) with 1 ns resolution. The tracer particles are silver-coated hollow glass spheres (SHGS) with an average diameter of $d_{\mathrm{avg,SHGS}} = 10\,\mu\mathrm{m}$. The camera takes 12 bit pictures with a frequency of about $2.5\,\mathrm{s}^{-1}$ and a resolution of $1910 \times 1483\,\mathrm{px}$ with respect to the rectangular size of the test section. The grid used for the estimation of the displacements of the particles has a size of 169×169 cells and is calibrated with an average factor of $150\,\mu\mathrm{m/px}$, covering three planar flow fields of $x/D \approx -3.0$ to 7.5 and $y/D \approx -4.0$ to 4.0

at $(z/D)_{large} \approx -2.72$, $(z/D)_{middle} \approx 0$ and $(z/D)_{small} \approx 2.72$. In order to generate one phase-resolved position (see Section 4), around 100 measurements are taken. Preliminary studies with more and fewer measurements showed that this number of 100 measurements represents a good compromise between accuracy and effort.

3.2.2 Laser Distance Sensor

In order to be able to capture the 3D structural deflections, a non-contact measurement method based on a laser distance sensor is applied. A laser triangulation technique is chosen because of the known geometric dependencies, the high data rates, the small measurement range and the resulting higher accuracy in comparison with other techniques such as laser phase-shifting or laser interferometry. The laser triangulation method is based on a laser beam which is focused onto the deformable object. A part of the light is reflected to a CCD-chip, located near the laser. When the object deforms itself, the distance between it and the sensor varies. This is detected on the CCD-chip. With this change on the CCD-chip and an internal length calibration adjusted to the applied measurement range, the deformation of the structure is calculated. To study simultaneously more than one point of the structure, a multiple-point triangulation sensor is applied (Micro-Epsilon scanControl 2750, see Fig. 4). This sensor uses a matrix of CCD chips to detect the displacements on up to 640 points along a laser line reflected on the surface of the structure with a data rate of 800 profiles per second. The laser line is positioned in a horizontal ($x/D \approx 3.1$, see Fig. 4(a)) and in a vertical alignment (see Fig. 4(b)) and has an accuracy of $40\,\mu$m. Due to the different refraction indices of air, glass and water a custom calibration is performed to take the modified optical behavior of the emitted laser beams into account.
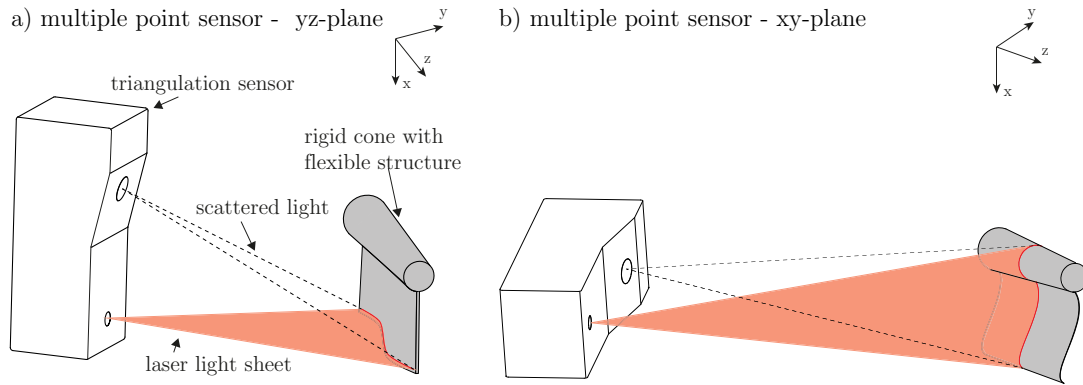

Figure 4: Setup and alignment of the multiple-point laser sensor on the flexible structure in a) yz-plane and b) xy-plane.

4 GENERATION OF PHASE-RESOLVED DATA

Each flow characteristic of a quasi-periodic FSI problem can be written as a function $f = \bar{f} + \tilde{f} + f'$, where $\bar{f}$ describes the global mean part, $\tilde{f}$ the quasi-periodic part and f' a random turbulence-related part (cf. [6, 16]). This splitting can also be written in the form $f = \langle f \rangle + f'$, where $\langle f \rangle$ is the phase-averaged part, i.e., the mean at constant phase. In order to be able to compare numerical results and experimental measurements, the irregular turbulent part f' has to be averaged out. Therefore, the present data are phase-averaged to obtain only the phase-resolved contribution $\langle f \rangle$ of the problem.

The present setup uses a reconstruction method for the phase averaging process. It consists of the multiple-point triangulation sensor (described in Section 3.2.2) and the synchronizer of the PIV system. Each measurement pulse of the PIV system is detected in the data acquisition of the laser distance sensor, which measures the structure deflection with a data rate of 800 profiles per second simultaneously with the PIV system.

The next steps for the post-processing of the experimental data are applied for each measurement plane separately and are processed as follows: Out of the structural data of the measurements in the three xy-planes ($z/D_{large} \approx -2.72$, $z/D_{middle} \approx 0$ and $z/D_{small} \approx 2.72$) the last reliable measurable point ($x/D \approx 3.1$) near the edge of the structure is monitored. With the resulting displacements as a function of time the reference period of the structure movement of this plane is calculated as follows. For this purpose the zero-crossings from negative to positive values of the y-displacements represent the beginning of a period. Applied to the whole time series of y-displacements, this method provides the beginning and the end of all periods independent of their period length as displayed in Fig. 5(a). The next step is the calculation of the average period duration by arithmetically averaging all period lengths found in the previous step leading to the reference period duration. A first averaging step calculates the average y-displacements covering all available measuring data from the laser distance sensor in time and space. For this purpose each period of the swiveling motion with varying interval length is divided into 137 equidistant parts. For each individual part an average of the y-displacements is predicted resulting in a reference period consisting of 137 data points. With this fine decomposition allowing a detailed representation of the structure deformation, each part only contains a small number of flow measurements. Therefore, the time or phase-angle interval per part has to be enlarged by a second averaging step for the structure data. The reference period and all recorded periods are now split into n parts covering larger equidistant phase-angle intervals (Fig. 5(b)) than before.
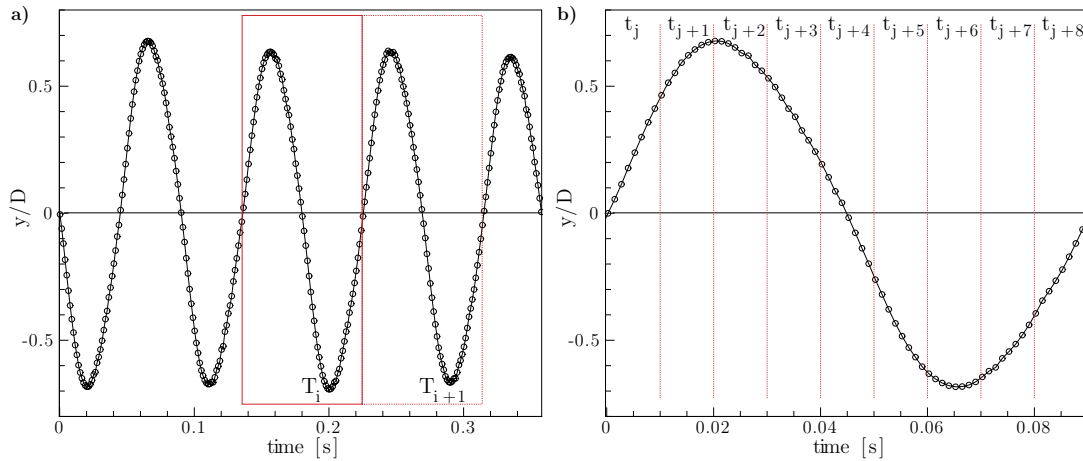

Figure 5: Phase-averaging procedure: (a) Period detection in y-displacements at a point near the trailing edge of the structure, (b) Period splitting into n parts (here for visibility only 9 parts) for the phase-averaging method.

In the present case n is set to 23 since it is a good compromise regarding a reasonable resolution of the phase-averaged motion and the number of measurements building each specific moment of the phase-averaged representation. A comparison of the corresponding 137 structure phase angles with the data of the newly defined reference period is performed for each part $n = 1$ to 23. The fluid and structure data of all matching profiles are assigned to the specific time-phase angle of the reference period, enabling the phase averaging of the PIV and structure

measurements. For the PIV experiments 2,000 single measurements per plane are taken. This is a compromise between the amount of data to be stored and the resulting post-processing costs and the limitations of the capture time of the laser distance sensor.

The phase-averaging procedure is also applied to the structure measurements in the yz-plane (see Fig. 4(a)) to receive simultaneous y-displacements in the monitored points z/D_{large}, z/D_{middle} and z/D_{small}. With these post-processing steps three separate phase-averaged reference structure and flow periods in the xy-plane and a single phase-averaged structure reference period in the yz-plane are obtained. A last post-processing step is necessary due to the phase-shift of the flow and structure movement between the three planes. Based on the phase-averaged results of the structural measurements in the yz-plane (see Fig. 4(a)) the precise phase shift between the planes is calculated. The displacements on the plane at the large cone diameter ($(z/D)_{large} \approx -2.72$) are chosen to define the beginning and end of the reference period. Afterwards, the calculated phase shifts are separately applied to the phase angles of the flow fields in the three xy-planes.

5 RESULTS AND DISCUSSION

5.1 Deflection of the Structure

Similar to a flow around a cylinder, the flow behind a single truncated cone creates a von Kàrmàn vortex street. Several studies [15, 14, 11] describe different vortex shedding frequencies along the cone axis according to the three-dimensional geometry. This leads to a splitting of vortices (or vortex dislocation) in the wake behind the small cone diameter and therefore to a complex and fully three-dimensional flow. Furthermore, the size of the vortices are directly dependent on the local cone diameter. Nevertheless, in the present case the rubber plate acts like a splitter plate [2] and modifies the flow behavior in a significant way. The movement of the plate suppresses the different vortex shedding frequencies along the cone leading to only one shedding frequency like in the wake of a cylinder. Nevertheless, the influence of the linearly increasing cone diameter is still present in the flow field. The three-dimensional flow with wide vortices behind the large cone diameter and smaller vortices on the other side, induces inhomogeneous pressure forces on the rubber plate. Due to the periodic and alternating shedding of vortices this effect is also time-dependent and creates a wavelike deformation of the rubber plate (see Fig. 6).
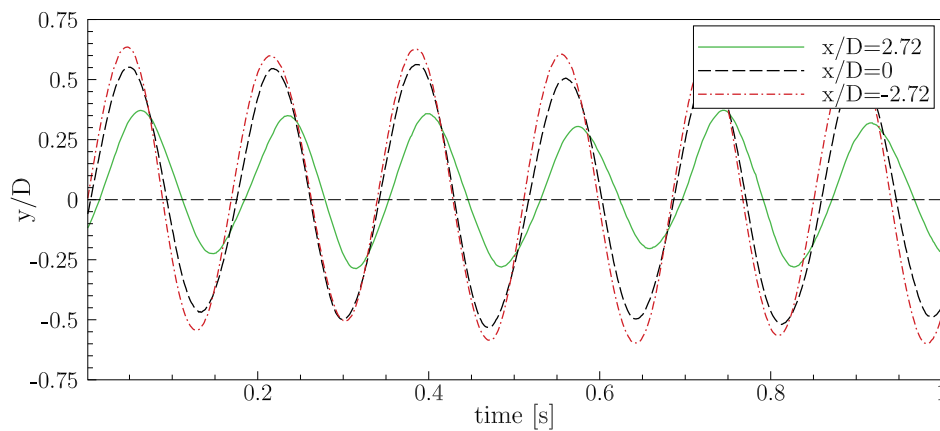

Figure 6: Structural results: raw signal of the deflection of the rubber plate at $(z/D)_{large} \approx -2.72$, $(z/D)_{middle} \approx 0$ and $(z/D)_{small} \approx 2.72$ measured in the yz-plane.

Summarizing these effects the FSI problem is quasi-periodic but fully three-dimensional with large structure deformations in negative z-direction (large cone diameter) and smaller deflections in positive z-direction (small cone diameter). In Fig. 6 the displacements of the structure within a time interval of one second (raw data) is presented. The plot is based on the displacement of three points located at the surface of the rubber plate and in a distance of 3 mm ($x/D = 3.1$) from the shell extremity. This point is chosen due to the measuring limitations of the structure sensor in resolution and illumination. The time series of these three displacement plots reveal cycle-to-cycle variations regarding the displacement amplitude and the swiveling frequency. Furthermore, the phase shift mentioned above is clearly visible. The structure at the large cone diameter is leading the structural motion. The structure in the middle of the domain follows with a phase shift of about 10 degrees. Finally, the structure at the small diameter reaches the same state with a phase delay of about 33 degrees with respect to the large diameter.
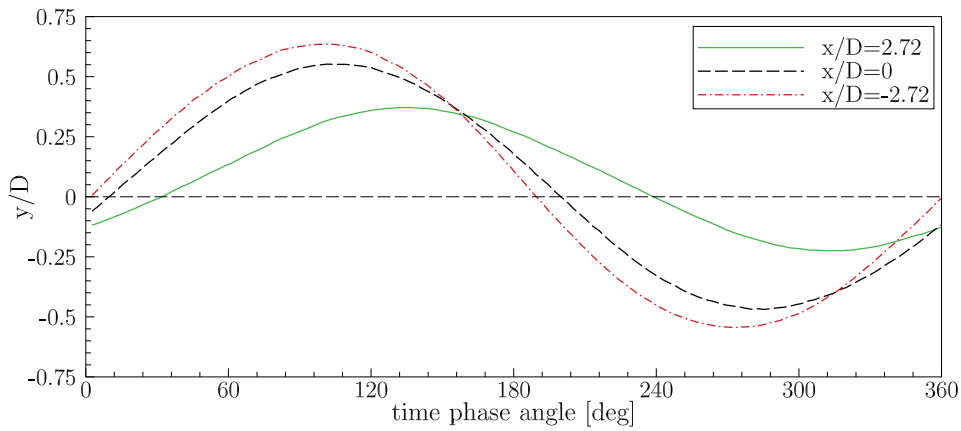

Figure 7: Structural results: phase-averaged period of the deflection of the rubber plate at $(z/D)_{large} \approx -2.72$, $(z/D)_{middle} \approx 0$ and $(z/D)_{small} \approx 2.72$.

In order to allow a quantitative comparison between the experimental results and numerical data all results are phase-averaged as explained in the previous section. With this process the mean period of the FSI phenomenon in flow and structure is generated. The results for the structure are presented in Fig. 7 for the three planes and in Fig. 8 for the entire line along the extremity. Based on the phase-averaged period of the deflections depicted in Fig. 7 the phase shift between the different planes is even more clearly visible. The phase difference between the small and middle diameter is significantly larger than between the middle and the large diameter. Thus the wave speed of the structural deflections in z-direction is not constant, which can be explained by minor pressure forces on this part ($z/D > 0$) of the structure and thus lower deformation rates there. Furthermore, the difference in the amplitudes also visibly differs between the small and the middle diameter compared to the middle and the large diameter.

The mentioned differences in the displacements along the truncated cone axis with mean extrema of the displacement are presented in Table 2. On first sight, the results in Figs. 7 and 8 seem to be not symmetric. But this asymmetry mainly occurs by the chosen measuring point on the surface of the structure. In Table 2 the measured mean y-displacements and those calculated for the chord are confronted. With respect to the calculated point at the chord of the structure the displacements are nearly symmetric. The remaining deviations from symmetry are perhaps caused by the slightly anisotropic material behavior of the rubber. The frequency of the FSI
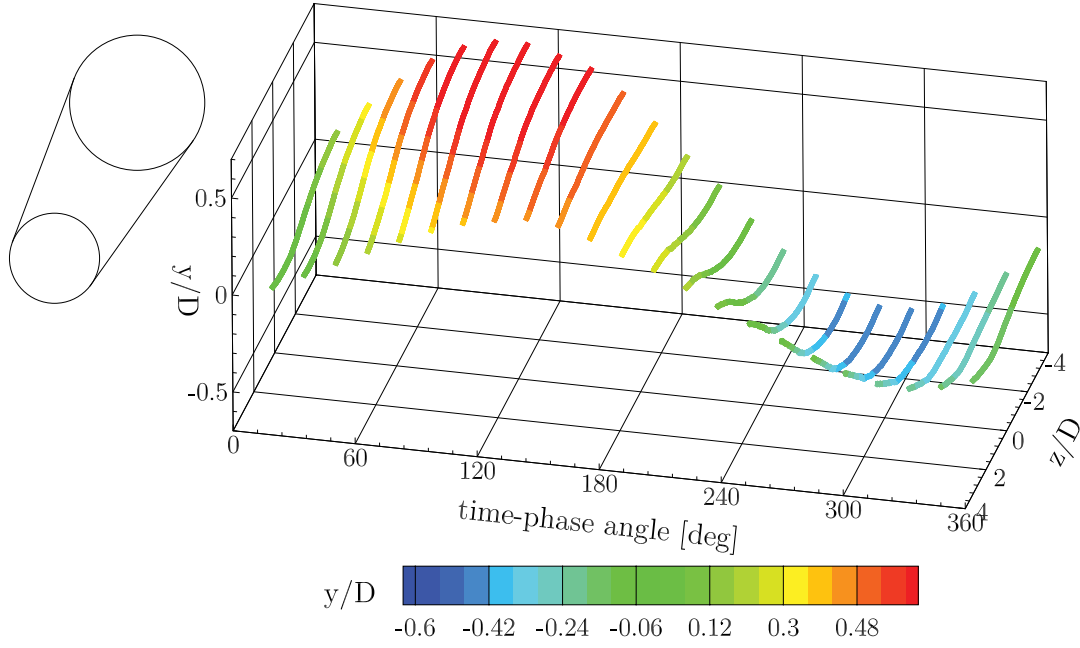
Figure 8: Structural results: phase-averaged period of the deflection of the rubber plate in the yz-plane near to the extremity of the structure (cone not in scale).

phenomenon, i.e., the frequency of the y-displacements, is about $f = 5.82\,\text{Hz}$ which correspond to Strouhal numbers of $St_{large} \approx 0.20$, $St_{middle} \approx 0.17$ and $St_{small} \approx 0.13$, respectively.

plane	$(y/D)_{max}$ large	$(y/D)_{min}$ large	$(y/D)_{max}$ middle	$(y/D)_{max}$ middle	$(y/D)_{max}$ small	$(y/D)_{max}$ small
point at surface	0.635	-0.543	0.551	-0.469	0.372	-0.225
point at chord	0.59	-0.588	0.506	-0.514	0.327	-0.270

Table 2: Measured (surface) and calculated (chord) mean y-displacements.

In Fig. 9 the phase-averaged deflections in the three xy-planes and the displacements in the yz-plane are merged into a three-dimensional mesh, illustrating the three-dimensional deformation of the rubber plate. At a phase angle of 16 degree the deflections all over the rubber plate are small. In the further movement at 78 degree the displacements at the larger diameter nearly reach their maximum, where in positive z/D-direction (small cone diameter) only small deflections are noticeable. This part catches up at the next phase angle shown for 141 degree where the displacements on the extremity are almost constant in z-direction. The following phase angles at 203, 266 and 329 degrees depict similar states of the structure movement in the opposite direction.
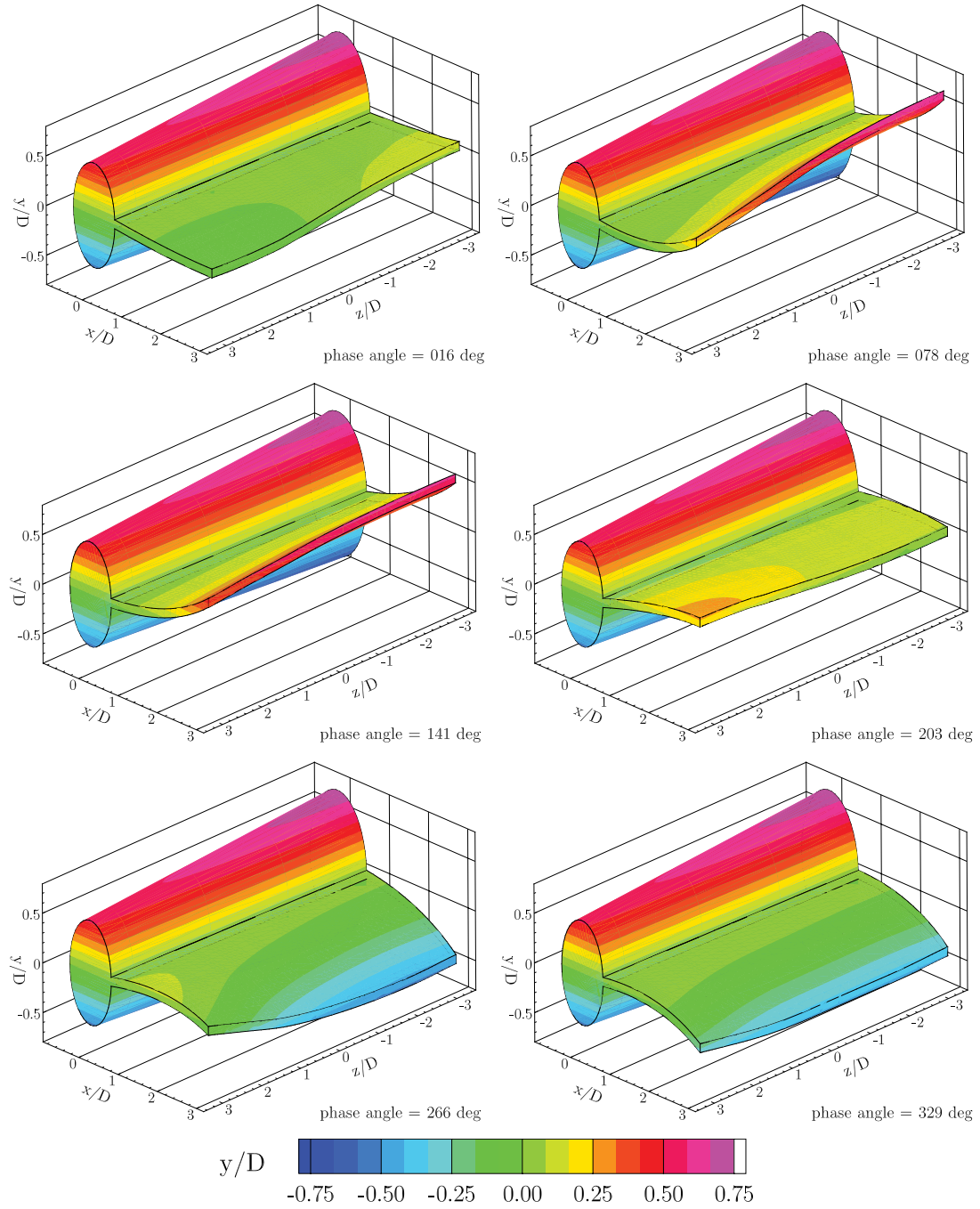
Figure 9: Structural results: interpolated and phase-averaged three-dimensional structure deformations for the reference period (note the axis ratio $(y/D)/(x/D) = 2$).

5.2 Flow Field

A selection of phase-averaged flow fields is depicted in Fig. 10. These six states of the mean period of the FSI problem illustrate the significant three-dimensional characteristic of the flow. The shed vortices are convected downstream leading to an alternating vortex pattern in the wake of the structure. In the wake of the structure the characteristic recirculation areas are observed. Finally, the shed vortices leave the region of interest. All planes ($(z/D)_{large} \approx -2.72$, $(z/D)_{middle} \approx 0$ and $(z/D)_{small} \approx 2.72$) at a single phase angle show the distinctive behavior

of this wake vortex. Nevertheless, compared to each other the three planes differ in the vortex size and the area of the wake influenced. The shed vortex on the plane $(z/D)_{large} \approx -2.72$ is much larger in size and velocity magnitude than on the plane $(z/D)_{small} \approx 2.72$. Also the mentioned phase shift between the large and the small cone diameter is visible through the staggered location of the vortex centers.
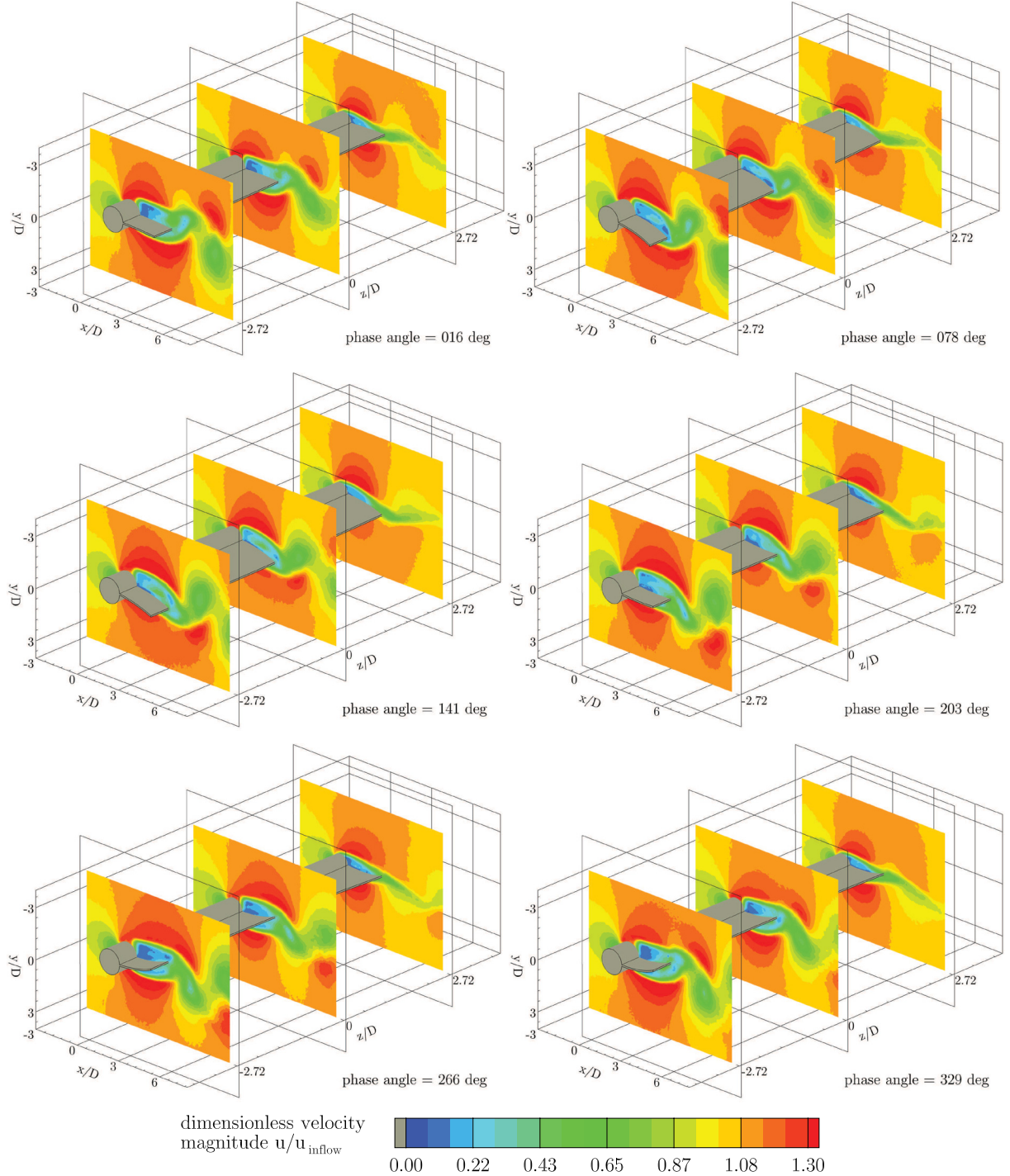

Figure 10: Phase-averaged PIV and structure results for the reference period.

6 CONCLUSIONS AND OUTLOOK

The paper presents a new three-dimensional FSI benchmark case denoted FSI-PfS-3a. The structure consists of a rigid truncated cone and a flexible membranous rubber tail fixed at the backside of the cylinder. According to the cone the flow is in the subcritical regime ($Re_{D1} = 2.1 \cdot 10^4$ or $Re_{D2} = 3.2 \cdot 10^4$). The FSI problem shows a quasi-periodic but fully three-dimensional behavior with larger structure deformations for increasing cone diameter. The detailed experimental investigations using optical measurements techniques for both, the fluid flow and the structure deformation, deliver comprehensive data for a reasonable validation process of FSI simulation tools.

7 AVAILABLE DATA FOR COMPARISON

This benchmark FSI-PfS-3a should help to evaluate and improve numerical FSI codes. Therefore, our department supports all interested groups with the experimental data presented in this paper and the first contribution to this session. Available for comparison are the 23 single phase-averaged two-dimensional reference velocity fields of the PIV measurement series at the three planes mentioned. For the flexible structure the raw and phase-averaged data of the displacements can be provided. Furthermore, static and dynamic material tests not mentioned in the paper are also available to prove the structural modeling. All data are stored in ASCII and Tecplot formats. Please contact the authors for more information or visit our website http://www.hsu-hh.de/pfs (see Section "Forschung/Fluid-Struktur-Wechselwirkung") for additional content (e.g., pictures, movies) concerning this and all other FSI benchmarks.

REFERENCES

[1] R. J. Adrian. Particle-imaging techniques for experimental fluid mechanics. *Annual Review of Fluid Mechanics*, 23(1):261–304, 1991.

[2] E.A. Anderson and A.A. Szewczyk. Effects of a splitter plate on the near wake of a circular cylinder in 2 and 3-dimensional flow configurations. *Experiments in Fluids*, 23(2):161–174, 1997.

[3] M. Breuer, G. De Nayer, M. Münsch, T. Gallinger, and R. Wüchner. Fluid-structure interaction using a partitioned semi-implicit predictor-corrector coupling scheme for the application of large-eddy simulation. *Journal of Fluids and Structures*, 29:107–130, 2012.

[4] M. Breuer and A. Kalmbach. Experimental investigations on fluid-structure interactions based on particle-image velocimetry. In A. Thess, C. Resagk, B. Ruck, A. Leder, and D. Dopheide, editors, *Proc. der 19. Gala–Fachtagung 'Lasermethoden in der Strömungsmesstechnik', Sept. 6–8, 2011*, pages 35–1–35–8, Universität Ilmenau, 2011.

[5] H.-J. Bungartz, M. Mehl, and M. Schäfer, editors. *Fluid Structure Interaction II: Modelling, Simulation, Optimization*, volume 73 of *Lecture Notes in Computational Science and Engineering, LNCSE*. Springer, Heidelberg, 2010.

[6] B. Cantwell and D. Coles. An experimental study of entrainment and transport in the turbulent near wake of a circular cylinder. *Journal of Fluid Mechanics*, 136(1):321–374, 1983.

[7] G. De Nayer, A. Kalmbach, M. Breuer, S. Sicklinger, and R. Wüchner. A fluid-structure interaction benchmark in turbulent flow (FSI-PfS-1a) – A complementary numerical/experimental investigation. *Journal of Fluids and Structures*, 2013. submitted.

[8] J. P. Gomes and H. Lienhart. Experimental study on a fluid-structure interaction reference test case. In H.-J. Bungartz and M. Schäfer, editors, *Fluid-Structure Interaction – Modelling, Simulation, Optimization*, volume 53 of *Lecture Notes in Computational Science and Engineering, LNCSE*, pages 356–370. Springer, Heidelberg, 2006.

[9] J. P. Gomes and H. Lienhart. Experimental benchmark: Self-excited fluid-structure interaction test cases. In H.-J. Bungartz, M. Mehl, and M. Schäfer, editors, *Fluid-Structure Interaction II – Modelling, Simulation, Optimization*, volume 73 of *Lecture Notes in Computational Science and Engineering, LNCSE*, pages 383–411. Springer, Heidelberg, 2010.

[10] J. P. Gomes and H. Lienhart. Fluid-structure interaction-induced oscillation of flexible structures in laminar and turbulent flows. *Journal of Fluid Mechanics*, 715:537–572, 2013.

[11] C.S. Jagadeesh. Dynamics of vortex shedding from slender cones. *Ph.D. thesis*, 2009. Queen Mary University of London.

[12] A. Kalmbach and M. Breuer. Investigations on fluid-structure interactions using volumetric particle-image velocimetry. In *16th Int. Symp. on Applications of Laser Techniques to Fluid Mechanics, July 09-12, 2012, Lisbon, Portugal*, 2012.

[13] A. Kalmbach and M. Breuer. Experimental PIV/V3V measurements and numerical RANS predictions of vortex-induced fluid-structure interaction in turbulent flow – A new benchmark FSI-PfS-2a. *Journal of Fluids and Structures*, 2013. submitted.

[14] V.D. Narasimhamurthy, H.I. Andersson, and B. Pettersen. Cellular vortex shedding behind a tapered circular cylinder. *Physics of Fluids*, 21:044106.1 – 044106.12, 2009.

[15] P.S. Piccirillo and C.W. van Atta. An experimental study of vortex shedding behind linearly tapered cylinders at low Reynolds number. *Journal of Fluid Mechanics*, 246:163–195, 1993.

[16] W. C. Reynolds and A. Hussain. The mechanics of an organized wave in turbulent shear flow. Part 3. Theoretical models and comparisons with experiments. *Journal of Fluid Mechanics*, 54(2):263–288, 1972.

[17] S. Turek and J. Hron. Proposal for numerical benchmarking of fluid-structure interaction between an elastic object and laminar incompressible flow. In H.-J. Bungartz and M. Schäfer, editors, *Fluid-Structure Interaction*, volume 53 of *Lecture Notes in Computational Science and Engineering, LNCSE*, pages 371–385. Springer, Heidelberg, 2006.

[18] S. Turek, J. Hron, M. Razzaq, H. Wobker, and M. Schäfer. Numerical benchmarking of fluid-structure interaction: A comparison of different discretization and solution approaches. In H.-J. Bungartz, M. Mehl, and M. Schäfer, editors, *Fluid-Structure Interaction II – Modelling, Simulation, Optimization*, volume 73 of *Lecture Notes in Computational Science and Engineering, LNCSE*, pages 413–424. Springer, Heidelberg, 2010.